



Bimetallic Co–Ni alloy nanoparticles loaded on nitrogen-doped wrinkled carbon nanospheres as high-performance bifunctional ORR/OER electrocatalyst in alkaline media

Qiuping Zhao^{1,2} · Lixia Bao^{1,2} · haibing Wang^{1,2} · Di Dou^{1,2} · Yuanyuan Cong^{1,2} · Chunlei Li^{1,2}

Received: 21 November 2023 / Revised: 9 March 2024 / Accepted: 13 March 2024 / Published online: 23 May 2024
© The Author(s), under exclusive licence to Springer-Verlag GmbH Germany, part of Springer Nature 2024

Abstract

Preparation of an advanced bifunctional oxygen electrocatalyst is important for fuel cells, water splitting, etc. Herein, we report an oxygen reduction reaction (ORR)/oxygen evolution reaction (OER) electrocatalyst with CoNi alloy nanoparticles uniformly distributed on nitrogen-doped carbon (N–C) nanospheres through a simple melamine-assisted pyrolysis strategy, in which a soft template approach is employed to prepare wrinkled N–C nanospheres. The Co₃Ni₁-N–C electrocatalyst exhibits higher onset potential ($E_0 = 0.960$ V vs. RHE (Reversible hydrogen electrode)), half-wave potential ($E_{1/2} = 0.81$ V vs. RHE), and limiting diffusion current ($j_L = 5.5$ mA cm⁻²) for ORR. Meanwhile, Co₃Ni₁-N–C electrocatalyst has a lower overpotential of 0.360 V vs. RHE at 10 mA cm⁻² for OER, and a lower value for Tafel slope of 100 mV dec⁻¹, a potential difference between OER and ORR ($\Delta E = E_{j=10} - E_{1/2}$) with a ΔE value of 0.779 V vs. RHE, which is close to the benchmark ΔE value of the combination of commercial noble metal catalysts (Pt/C–RuO₂, 0.744 V vs. RHE). In addition, Co₃Ni₁-N–C also shows remarkable stability, maintaining a relative current of 81.45% after 10 h at 0.8 V. The relative current of Co₃Ni₁-N–C is also found to be stable, superior to commercial Pt/C by 34.5%. These excellent properties are due to its unique wrinkled structure, large surface area, and high content of CoNi-N_x and pyridine nitrogen active centers.

Keywords Nitrogen-doped carbon nanospheres · Non-noble metal oxygen reduction reaction · Oxygen evolution reaction

Introduction

Environmental problems are becoming more and more serious due to the continuous consumption of fossil energy sources. One potential approach is to replace fossil fuels with sustainable and clean energy sources [1–3]. Devices that convert and store energy using electrochemistry are effective, dependable, and eco-friendly (such as metal-air batteries, fuel cells, water splitting, and solar fuel synthesis) [4], and they have grown to play a significant role in modern energy systems [5, 6]. Oxygen reduction reaction (ORR) and oxygen evolution reaction (OER) are the key electrode

reaction processes of these new energy systems [7–9]. However, due to kinetic retardation in both the ORR and OER processes [10], electrocatalysts are essential to catalyze the ORR/OER reaction pathway [11, 12]. Currently, non-precious metals and their oxides, such as platinum (Pt), iridium oxide (IrO₂) and ruthenium oxide (RuO₂), have been shown to be the best electrocatalysts for ORR/OER. Unfortunately, the high cost and scarcity of resources of these precious metals, as well as poor multifunctional catalytic properties, have greatly limited their commercialization process [13–15]. Therefore, over the past years, intense investigations have been devoted to explore low-cost and efficient ORR/OER electrocatalyst based non-precious metals [16]. Among them, nitrogen-coordinated transition metal alloys (M–N–C, M = transition metal alloys such as NiCo [8], FeCo [10], and NiFe [17]) supported on carbon carriers are considered a promising candidate for enhancing OER/ORR activity. The design of M–N–C materials relies on atomically dispersed M–N_x sites and excellent carbon structure, and the rational carbon structure is favorable for the exposure of active sites and enhancement of mass transfer to improve the ORR/OER

✉ Chunlei Li
licl@lut.edu.cn

¹ Key Laboratory of Low Carbon Energy and Chemical Engineering of Gansu Province, Lanzhou University of Technology, Lanzhou 730050, Gansu, China

² School of Petrochemical Technology, Lanzhou University of Technology, Lanzhou 730050, Gansu, China

performance. Among them, CoNi alloys not only provide a rich variety of valence changes, but also induce change in surface properties and intrinsic polarity during oxygen reactions. The combination of bimetallic CoNi alloys and N-doped carbon promotes OER and ORR reaction kinetics. For example, Chen et al. [8] synthesized CoNi alloy nanoparticles on carbon nanofibers with unique pomegranate-like morphology and microstructure, which exhibited excellent OER and ORR electrocatalytic activities. Singh et al. [18] developed NiCo alloys supported by porous graphene and exhibited excellent OER activity. However, agglomeration of the alloy nanoparticles and direct exposure to the electrolyte inevitably lead to a decrease in catalytic activity and stability. In addition, the alloy nanoparticles tend to leach from the surface of the carbon matrix due to oxidative degradation of carbon. Therefore, encapsulation of CoNi nanoparticles into N-doped carbon layers to form a porous carbon sphere structure is a potential strategy to improve the catalytic performance, in which the highly conductive N-doped carbon layer has a protective shell against agglomeration and oxidation/corrosion of the alloy nanoparticles under harsh operating conditions [19]. More importantly, the strong interaction between the metal active center and the N-doped carbon layer effectively modulates the electronic structure of the outer carbon layer while improving the reaction kinetics [20]. The porous carbon nanospheres structure prevents the collapse of the whole structure during the OER/ORR process, and the porous structure provides abundant active sites for the catalytic reaction [21, 22]. Compared with previously reported CoNi-N-C electrocatalysts with irregular carbon structure, carbon nanosphere electrocatalysts with porous structure not only stabilize the CoNi-N_x active sites due to the special larger surface area, but also prevent chronic aggregation in the practical application of stabilized structure [23, 24]. Metal co-doped porous carbon nanospheres electrocatalysts have high activity and stability in oxygen electrocatalysis [25]. In addition the electrocatalysts synthesized using melamine assistance can be doped into the precursors as a nitrogen source, giving them a large number of active sites [26]. Therefore, the modulation of the active sites of carbon nanosphere electrocatalysts using melamine provides a new approach for the preparation of high-performance advanced carbon materials. Therefore, modulation of the active sites of carbon nanosphere electrocatalysts using melamine provides a new approach for the preparation of high-performance advanced carbon materials.

Here, we synthesized a wrinkled-containing nitrogen-doped carbon nanospheres using a soft template method, followed by the addition of cobalt and nickel salts. The doping of melamine to provide a nitrogen source during pyrolysis improved the distribution of active sites, and its large surface area and high content of M-N_x active sites promoted ORR activity and accelerated the surface reconstruction layer to

achieve high OER performance [27]. The effects of different molar ratios of Co (NO₃)₂·6H₂O and Ni(NO₃)₂·6H₂O on the ORR/OER performances were investigated and compared with those of commercial catalysts, and the obtained Co_xNi_y-N-C electrocatalysts showed good ORR/OER activities. The as-obtained Co₃Ni₁-N-C electrocatalyst exhibited favorable ORR, OER activity with a half-wave potential of 0.81 V vs. RHE and an onset potential of 0.960 V vs. RHE. The OER overpotential η_{10} at 10 mA cm⁻² was 360 mV, which was only 11 mV lower than the overpotential of commercial RuO₂. In addition, the Co₃Ni₁-N-C electrocatalyst showed better stability in 0.1 M KOH solution also showed better stability. These results suggested that the optimization of the carrier structure and the combination of melamine as a nitrogen source to modulate the active sites of the bimetallic composites was a promising strategy to improve the ORR and OER properties.

Experimental component

Materials

Dopamine hydrochloride (purity ≥ 98.0%), 1,3,5-trimethylbenzene (TMB, purity ≥ 98.0%), and ammonia (purity ≥ 28.0%) were obtained from Aladdin Biochemical Technology Co. Ltd (Shanghai, China). Pluronic F127 (purity, BR) and melamine (purity ≥ 99.0%) were obtained from McLean Biochemical Co. Ltd. (Shanghai, China). Cobalt nitrate hexahydrate (Co(NO₃)₂·6H₂O) (purity ≥ 98.5%), nickel nitrate hexahydrate (Ni(NO₃)₂·6H₂O) (purity ≥ 98.0%), potassium hydroxide (KOH) (purity ≥ 85.0%), and sodium hydroxide (NaOH) (purity ≥ 96.0%) were purchased from Sinopharm Chemical Reagent Co. Ltd. (Shanghai, China). Platinum carbon (JM Pt/C) catalyst (20 wt%) was obtained from Johnson Matthey Chemical Co. Ltd. (Landon, UK) and ruthenium dioxide (RuO₂) catalyst was obtained from Sigma Aldrich Trading Co. Ltd. (purity ≥ 99.0%) (Shanghai, China). Ultrapure water (18.2 MΩ•cm at 25 °C) was used for all experiments.

Preparation of Co_xNi_y-N-C

In a typical Co_xNi_y-N-C synthesis, 0.6 g of dopamine hydrochloride, 0.4 g of Pluronic F127 (F127), and 1.6 mL of 1,3,5-trimethylbenzene (TMB) were dispersed in a mixture of 20 mL of water and 20 mL of ethanol and sonicated for 30 min to bring it to an emulsion. Subsequently, 1.5 mL of ammonia was rapidly added to the above solution at 25 °C with stirring. After 2 h of reaction, the product was centrifuged at 12,000 rpm for 10 min and washed with ethanol/water mixture, and the process was repeated three times. The collected products were then dried at 80 °C and

then heated from room temperature to 800 °C at a heating rate of 5 °C min⁻¹ in an N₂ atmosphere and held for 2 h to obtain carbon nanosphere carriers. The prepared carbon nanosphere carriers (100 mg) were dispersed in 10 mL of a mixed solution of X mmol of cobalt nitrate hexahydrate (Co(NO₃)₂·6H₂O) (X = 0.217 mmol, denoted by x = 3) and Y mmol of nickel nitrate hexahydrate (Ni(NO₃)₂·6H₂O) (Y = 0, 0.072, 0.144, and 0.217 mmol, denoted by y = 0, 1, 2, 3, respectively) in a mixed solution of water. After sonication for 30 min, the mixture was transferred to a 50 °C water bath and held for 2 h, in which the Co and Ni salts were uniformly loaded on the carriers. The temperature was then raised to 100 °C, and the aqueous mixed solution was eventually removed as the temperature of the reaction system continues to rise. The precursors loaded with Co and Ni (75 mg) were homogeneously mixed with melamine (300 mg) by grinding in a mortar and pestle. Then, the mixture was annealed in N₂ atmosphere at a heating rate of 5 °C min⁻¹ from room temperature to 800 °C for 2 h. The final sample obtained was named Co_xNi_y-N-C. Co₀Ni₃-N-C was synthesized in the same way in a mixed solution of Ni(NO₃)₂·6H₂O (0.217 mmol) in water, and the method of N-C preparation was the same as that of Co_xNi_y-N-C, which was synthesized without the addition of melamine and metals.

Physical characterization

The measurements were taken using a Bruker D8 Advance diffractometer, Germany, and the X-ray diffraction (XRD) pattern was performed using Cu K radiation (40 kV, 100 mA, λ = 0.15432 nm) in the 2θ range, with a scanning range of 5–90° and a scanning rate of 5° min⁻¹. X-ray photoelectron spectroscopy (XPS) measurements were recorded on a Thermo Scientific K-Alpha spectrometer, USA, using an Al Kα source (hν = 1486.6 eV) with a constant passage energy of 20 eV. The binding energy was calibrated using a C1s of 284.8 eV as a reference. Transmission electron microscopy (TEM) images were performed under a FEI Talos F200x electron microscope at 200 kV. Scanning electron microscopy (SEM) was performed under a ZEISS Sigma 300 electron microscope in Germany. Raman spectra were collected on a Horiba LabRAM HR Evolution spectrometer in Japan with a Raman excitation wavelength of 532 nm. Quantachrome Autosorb IQ3, USA, was used for nitrogen isothermal adsorption and desorption test to measure the specific surface area of the material based on the adsorption properties of gases on solid surfaces, the physical adsorption of gas molecules by the sample particles under test at a specific temperature, and a fixed equilibrium adsorption amount under a certain pressure. By measuring its equilibrium adsorption amount, a theoretical model is used to calculate the specific surface area of the surface.

Electrochemical measurements

Electrochemical experiments were performed on a CHI-660 electrochemical workstation with a rotating disk electrodes (RDE) system (Pine Research Instruments). The working electrode was a glassy carbon (RDE diameter 5 mm, 0.196 cm²) with a deposited electrocatalyst layer, and the counter and reference electrodes were graphite rods and Hg/HgO (1 M NaOH) electrodes, respectively. The electrocatalyst ink was prepared by dispersing 5.0 mg of electrocatalyst in 30.0 μL of Nafion solution (5 wt%), 4.5 mL of ethanol, and 0.5 mL of water and ultrasonicated for 10 min. A 150 μL of ink was cast on the RDE with an electrocatalyst loading of 1.5 mg cm⁻² at the working electrode. For comparison, commercial Pt/C (20 wt%) and commercial RuO₂ inks were prepared in a similar way by casting 10 μL of ink onto RDE with a loading of 0.1 mg cm⁻² for JM Pt/C (20 wt%) and commercial RuO₂. All ORR and OER potentials reported in this study were converted to reversible hydrogen electrodes (RHE) by the conversion equations E(RHE) = E(Hg/HgO) + 0.895 V and E(RHE) = E(Hg/HgO) + 0.917 V, respectively, which were determined by equilibrium of the platinum disk electrodes as working electrodes in H₂-saturated 0.1 M KOH_{aq}. and 1 M KOH_{aq}. potentials were determined. Test cyclic voltammetry (CV) tests performed in 0.1 M KOH saturated with N₂ and O₂ at a sweep rate of 50 mV s⁻¹ with a voltage interval ranging from 0 to 1.2 V vs. RHE. ORR activity was evaluated by linear sweep voltammetry (LSV) in O₂-saturated 0.1 M KOH, the same as for CV ventilation, in a saturated nitrogen atmosphere, and LSV data were measured for the working electrodes at their different rotational speeds as a background current, ranging from 400, 900, 1600, 2025 to 2500 rpm, in that order. Subsequent operation under oxygen saturation was the same as under nitrogen. The voltage range was 0~1.20 V vs. RHE with a sweep rate of 10 mV/s. OER electrochemical tests were carried out in N₂-saturated 1 M KOH solution with CV at a sweep rate of 50 mV/s and a voltage range of 1.0~1.8 V vs. RHE. LSV was tested for OER activity at a sweep rate of 5 mV s⁻¹ and a rotational speed of 1600 rpm with a voltage range of 1.2~1.8 V vs. RHE. In the electrochemical active surface area (ECSA) test, the relative size of the ECSA of a sample material is determined by testing the size of its bilayer. The potential window for the CV test was 1.08~1.16 V vs. RHE, and the scanning speed was set to 20 mV s⁻¹, 40 mV s⁻¹, 60 mV s⁻¹, 80 mV s⁻¹, and 100 mV s⁻¹. Finally, by calculating and fitting a linear relationship between scanning speed and current density, the size of the bilayer of the sample material is the slope of the obtained line. The stability of the electrocatalysts in ORR and OER was carried out in O₂-saturated 0.1 M KOH solution and N₂-saturated 1 M KOH solution, respectively. The tests were carried out by the current–time (i–t) chronoamperometry

technique at voltages of 0.8 V vs. RHE and 1.6 V vs. RHE, respectively, at 1600 rpm for 10 h.

Calculation of electrochemical performance test data

Oxygen reduction reaction is a complex reaction with a multi-electron reaction process or a combination of four-electron and two-electron reactions as the reaction pathway. In order to better study its reaction kinetics, experiments were carried out using the rotating disk technique. The oxygen reduction process was calculated from the rotating disk electrodes (RDE) by the Koutecky-Levich (K-L) equation (Eqs. 1 and 2) [28]. The formula is as follows:

$$\frac{1}{j} = \frac{1}{j_L} + \frac{1}{j_K} = \frac{1}{B^{1/2}} + \frac{1}{j_K} \quad (1)$$

$$B = 0.62nF(D_0)^{2/3} \nu^{-1/6} C_0 \quad (2)$$

where j is the measured current density, j_K is the kinetic current density, j_L is the limiting current density, B determines the slope of the K-L plot, ω denotes the rate of rotation of the electrode expressed in rpm, F is Faraday's constant ($96,485 \text{ C mol}^{-1}$), C_0 is the volumetric concentration of O_2 ($1.2 \times 10^{-6} \text{ mol cm}^{-3}$), D_0 is the diffusion factor of 0.1 M KOH aq. ($1.9 \times 10^{-5} \text{ cm}^2 \text{ s}^{-1}$), and ν is the kinetic viscosity of the electrolyte ($0.01 \text{ cm}^2 \text{ s}^{-1}$).

Results and discussion

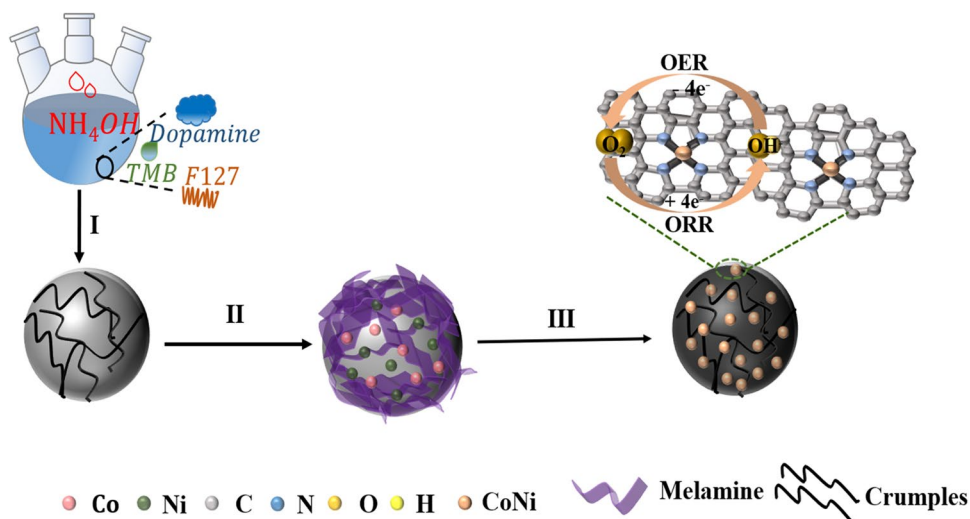
Structural features

The synthesis of $\text{Co}_x\text{Ni}_y\text{-N-C}$ carbon nanoballs electrocatalysts with different Co/Ni molar ratios with wrinkles was

assisted by the use of melamine as shown in Fig. 1. First, TMB was used as a nanoemulsion to polymerize and assemble dopamine hydrochloride in a mixed solution of water in the presence of ammonia. Then, F127 was used as a soft template to modulate the pore structure and surface texture of the polymerized complexes. As shown in Figs. S1a–b, the polymer maintained an intact blob morphology during centrifugation and washing, and the presence of abundant wrinkles in the polymer can be clearly seen. Second, the carbon nanosphere carriers were obtained after heat treatment of the polymers at $800 \text{ }^\circ\text{C}$ for 2 h under N_2 atmosphere, which still maintained the initial structure and spherical morphology, as shown in Figs. S1c–d. Carbon nanospheres enriched with N species were negatively charged and can adsorb cations (Co^{2+} and Ni^{2+}) from $\text{Co}(\text{NO}_3)_2 \cdot 6\text{H}_2\text{O}$ and $\text{Ni}(\text{NO}_3)_2 \cdot 6\text{H}_2\text{O}$, avoiding the detachment or agglomeration of metal species during annealing [29]. The powders loaded with Co and Ni salts were further milled with melamine, which was used as a nitrogen source to develop highly N-doped electrocatalysts. Finally, the mixture was annealed at $800 \text{ }^\circ\text{C}$ for 2 h in N_2 atmosphere, and the $\text{Co}_x\text{Ni}_y\text{-C-N}$ electrocatalyst was collected.

Firstly, the morphology and microstructure of $\text{Co}_3\text{Ni}_1\text{-N-C}$ were characterized by SEM and TEM; as shown in Fig. 2a–c, $\text{Co}_3\text{Ni}_1\text{-N-C}$ had a spherical morphology. And it can be seen in the SEM and TEM images that there were wrinkles on each nanosphere, and these wrinkles can effectively immobilize and disperse the active sites to prevent agglomeration [30]. No Co, Ni-based nanoparticles or nanoparticle clusters were found in the high-resolution transmission electron microscope, but the ones on $\text{Co}_3\text{Ni}_1\text{-N-C}$ have clear graphite stripes as shown in Fig. 2d. In addition, through the HAADF-TEM images and the corresponding elemental mapping images, it could be seen that there were uniformly distributed Co, Ni, C, and N elements in $\text{Co}_3\text{Ni}_1\text{-N-C}$ as shown in Fig. 2e–i. And there was a good

Fig. 1 Synthesis schematic diagram of $\text{Co}_x\text{Ni}_y\text{-N-C}$



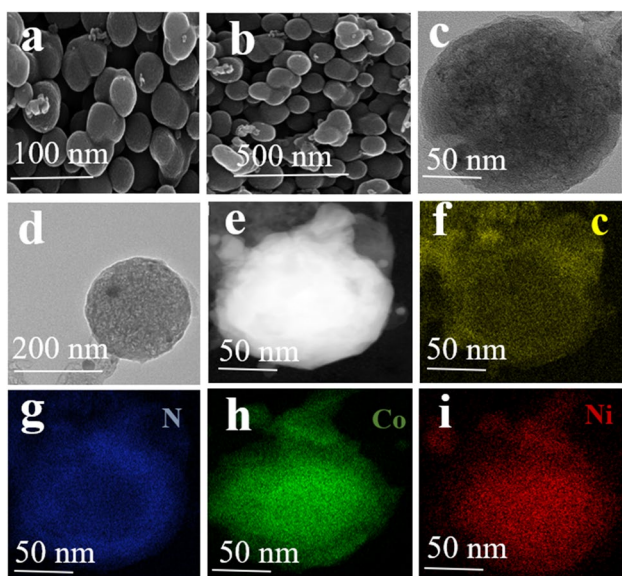


Fig. 2 SEM image (a–b), HR-TEM image (c), TEM image (d), HAADF-STEM images, and corresponding elemental mapping images (e–i) of $\text{Co}_3\text{Ni}_1\text{-N-C}$

overlap of Co and Ni, as shown in Fig. 2h–i, indicating the formation of CoNi alloy.

In order to optimize the synthesis scheme of $\text{Co}_x\text{Ni}_y\text{-N-C}$ catalysts, this paper focused on the Co/Ni molar ratio as an important influence on their catalytic activity. The crystal structures of $\text{Co}_x\text{Ni}_y\text{-N-C}$ prepared at 800 °C with different Co/Ni molar ratios were analyzed using X-ray diffractograms (XRD). As shown in the XRD plot in Fig. 3a, the relatively broad peak at 26.0° is the (002) plane of graphitic carbon. The characteristic peaks of the $\text{Co}_x\text{Ni}_y\text{-N-C}$ sample were located between the diffraction peaks of Co (PDF#15–0806) and Ni (PDF#04–0850), respectively, and according to previous reports, the peaks at 44.5°, 51.8°, and 76.2° correspond to the diffraction peaks of the face-centered cubic CoNi alloys at (111), (200), and (220) diffraction peaks [31]. Compared with $\text{Co}_3\text{Ni}_0\text{-N-C}$ and $\text{Co}_0\text{Ni}_3\text{-N-C}$, the $\text{Co}_x\text{Ni}_y\text{-N-C}$ diffraction peak (111) was shifted to the high angle direction with the increase of Ni content, which proved the successful doping of nickel elements and the formation of Co/Ni alloy, which led to the stretching of the crystalline spacing. The results showed that the peak intensity increases with increasing metal content, indicating that the degree of crystallization of the samples increased with increasing metal content [32].

The Raman spectroscopic characterization carried out to investigate the chemical structural state of the $\text{Co}_x\text{Ni}_y\text{-N-C}$ electrocatalyst was shown in Fig. 3c. All the samples had two distinct main peaks near 1342 cm^{-1} and 1589 cm^{-1} , indicating that they represented disordered carbon (from the D peak) and graphitic carbon (from the G peak), respectively,

and the intensity ratios of I_D/I_G can be used for evaluating the degree of graphitization and defects in the carbon arrays. The results by Raman spectroscopy showed that the metal content had a significant effect on the I_D/I_G ratio, where the I_D/I_G values of $\text{Co}_x\text{Ni}_y\text{-N-C}$ and $\text{Co}_3\text{Ni}_0\text{-N-C}$ ($I_D/I_G = 1.04$) and $\text{Co}_0\text{Ni}_3\text{-N-C}$ ($I_D/I_G = 1.02$) were less than that of N–C ($I_D/I_G = 1.09$), which indicated that the introduction of the metal improved the graphitization of the catalysts degree. Among $\text{Co}_x\text{Ni}_y\text{-N-C}$, its $\text{Co}_3\text{Ni}_1\text{-N-C}$ had the smallest ($I_D/I_G = 1.01$) value, indicating that $\text{Co}_3\text{Ni}_1\text{-N-C}$ had a higher degree of graphitization, which gave it a higher conductivity and promoted the electron transfer, and thus improved the electrocatalytic activity. Notably, the successful doping of Ni and Co elements and the presence of CoNi alloy in the catalyst samples were demonstrated by both Raman spectroscopy and XRD patterns. The structural properties of $\text{Co}_3\text{Ni}_1\text{-N-C}$ and N–C electrocatalysts were analyzed by N_2 adsorption–desorption isotherm (BET), as shown in Fig. 3c; $\text{Co}_3\text{Ni}_1\text{-N-C}$ and N–C exhibited type IV adsorption isotherms indicated the presence of mesoporous structure in $\text{Co}_3\text{Ni}_1\text{-N-C}$ [33]. In addition, the average pore size (11.51 nm), pore volume (0.29 $\text{cm}^3 \text{g}^{-1}$), and BET specific surface area (140.3 $\text{m}^2 \text{g}^{-1}$) of $\text{Co}_3\text{Ni}_1\text{-N-C}$ are shown in Fig. 3d–e and Table S1. This had mesoporous structure, large pore volume, and specific surface area, which could provide abundant active sites for the reaction, as well as convenient mass transfer conditions for ORR and OER catalytic processes. For N–C prepared without the introduction of metals, the pore volume and BET specific surface area were 0.10 $\text{cm}^3 \text{g}^{-1}$ and 21.9 $\text{m}^2 \text{g}^{-1}$, respectively (e.g., Table S1). Apparently, these results could be explained by the introduction of the metal, which facilitated the production of homogeneous nanoparticles and the increase of graphitization, and thus increased the pore volume/BET specific surface area. Upon comparison, it was shown that the doping of cobalt–nickel bimetallic could effectively increase the porosity and specific surface area of nitrogen-doped carbon nanorods, reduce the defects to increase the degree of graphitization, and improve the electrical conductivity of the catalysts; the enriched pore structure and high specific surface area were conducive to maximizing the exposure of the electrocatalytic active sites and facilitating the mass-transfer process in the reaction, which further enhanced the electrocatalytic performance of the materials.

The chemical composition and valence states of the surface elements of $\text{Co}_3\text{Ni}_1\text{-N-C}$ and N–C were characterized using X-ray photoelectron spectroscopy (XPS). As can be seen from Fig. 4a, the full spectrum of $\text{Co}_3\text{Ni}_1\text{-N-C}$ showed the presence of more Co and Ni elements compared to N–C. As shown in Fig. 4b, the high-resolution C 1s peaks of N–C and $\text{Co}_3\text{Ni}_1\text{-N-C}$ were analyzed with the same results. The high-resolution C 1s peaks at 284.8 eV, 285.6 eV, 288.9 eV, and 286.5 eV for $\text{Co}_3\text{Ni}_1\text{-N-C}$ and

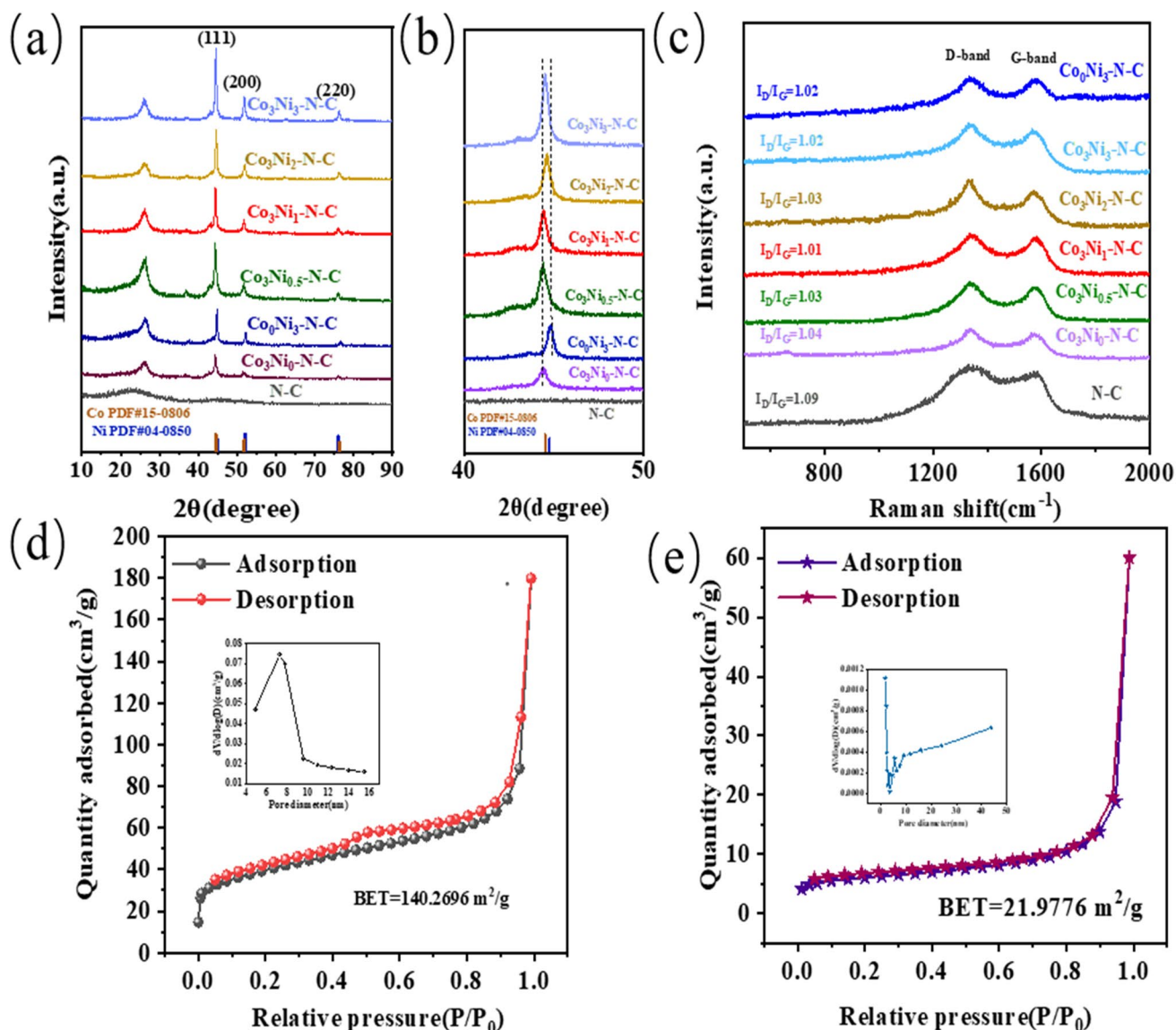


Fig. 3 XRD patterns (a, b) and Raman spectra (c) of the Co₃Ni₁-N-C and N-C electrocatalysts; N₂ adsorption–desorption isotherms and pore size distribution of the Co₃Ni₁-N-C and N-C electrocatalysts (d, e)

N-C were attributed to C–C, C–N, O–C–O, and C=O, respectively, where the C–N bond was the catalytically active site [8], and the presence of C–N bond confirmed the successful doping of nitrogen. Furthermore, the presence of N 1s spectra confirmed that the electrocatalyst was N-doped. As shown in Fig. 4(c), five characteristic peaks were decomposed in the Co₃Ni₁-N-C high-resolution N 1s spectrum: pyridine-N (398.2 eV), M-Nx (399.12 eV), pyrrole-N (400.7 eV), graphite-N (402.2 eV), and oxidized-N (405.4 eV) [34]. On the other hand, because no metal salts were introduced during the preparation procedure, as shown in Fig. 4c, N-C did not breakdown the M-Nx signal. It was possible that N and metal elements were successfully doped into the carbon matrix based on

the presence of N-C and M-Nx [35]. Among them, the formation of M-Nx site could accelerate the charge transfer and improve the electrochemical activity, which was an effective active site in the ORR/OER process. Also pyridine-N and graphite-N played a crucial role in the ORR/OER process by promoting oxygen adsorption while lowering the overpotential due to their superior electron acceptance [36]. The contents of different N species in Co₃Ni₁-N-C and N-C were calculated by XPS tests as shown in Fig. 4f, where the total N content of Co₃Ni₁-N-C increased to 4.22 at%, while N-C was 2.9 at%. In addition, the pyridine-N content in Co₃Ni₁-N-C was much higher than that in N-C, indicating that the melamine-assisted synthesis strategy increased the number of active sites.

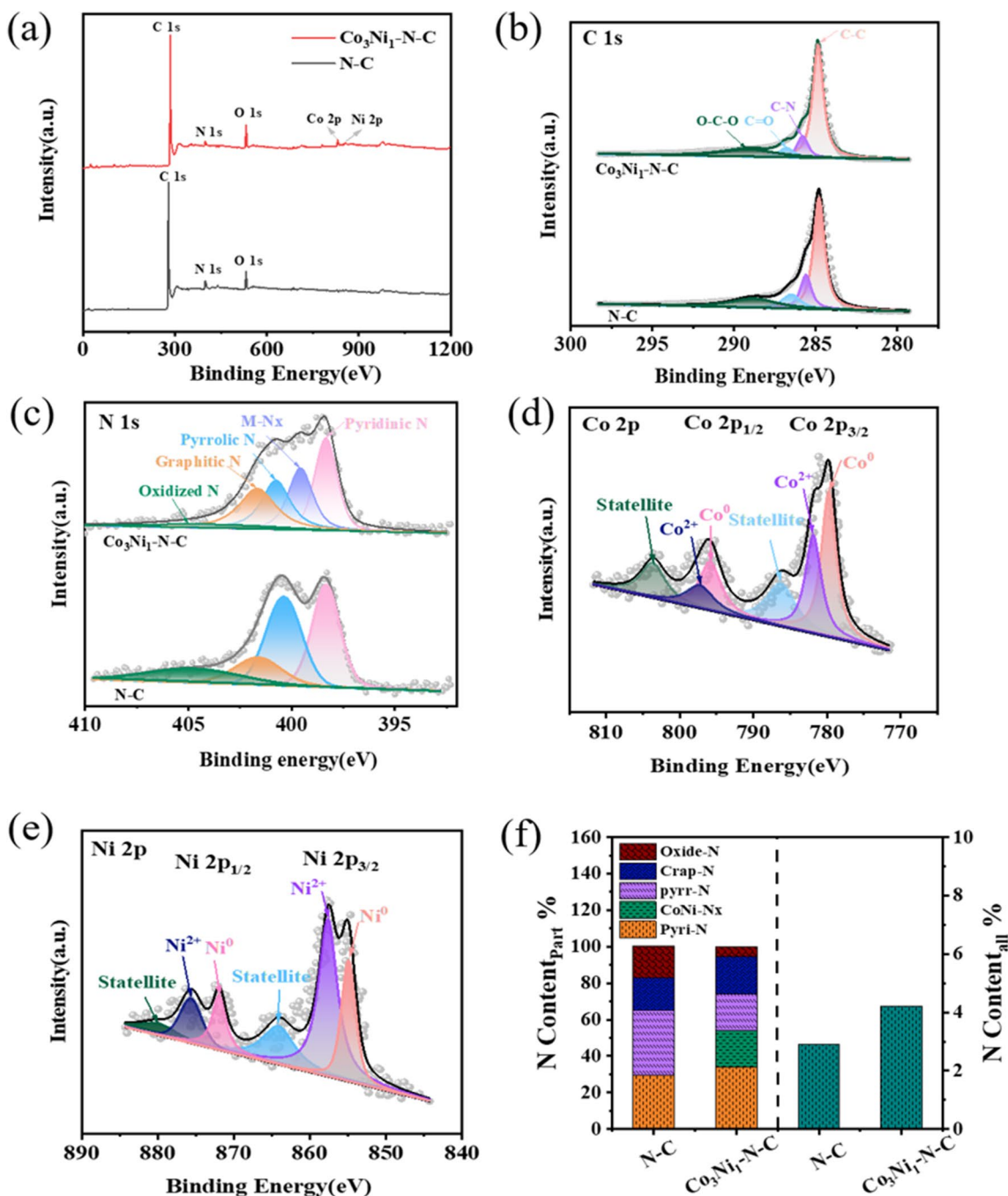


Fig. 4 XPS full spectrum peaks of $\text{Co}_3\text{Ni}_1\text{-N-C}$ and N-C (a); C 1 s peaks of $\text{Co}_3\text{Ni}_1\text{-N-C}$ and N-C (b); high-resolution XPS spectra of N 1 s peaks of $\text{Co}_3\text{Ni}_1\text{-N-C}$ and N-C (c); Co 2p peaks (d); high-resolu-

tion XPS spectra of Ni 2p peaks (e); calculation of the XPS results for $\text{Co}_3\text{Ni}_1\text{-N-C}$ and N-C carbon matrices for different nitrogen species and nitrogen elements (f)

Except for the oxidized-N species, all the other four N groups had important effects on the catalytic ORR/OER [37].

In the XPS Co 2p spectrum, as shown in Fig. 4d, the peaks at 780.3 and 796.8 eV are Co 2p_{3/2} and Co 2p_{1/2}, respectively. Peaks located at 784.2 and 802.9 eV indicated satellite peaks. In addition, the 780.0 and 796.1 eV peaks

were attributed to the metallic Co peaks. the N-coordinated Co²⁺ peaks at 781.8 and 797.2 eV [38] indicated that the Co particles were anchored to the NC substrate. The XPS Ni 2p spectra are shown in Fig. 4e similar to Co, but with lower Ni content than Co [39]. The 855.3 and 873.2 eV peaks correspond to the metallic Ni peaks, and 856.4 and 875.1 eV peaks correspond to the Ni²⁺ peaks. Finally, the

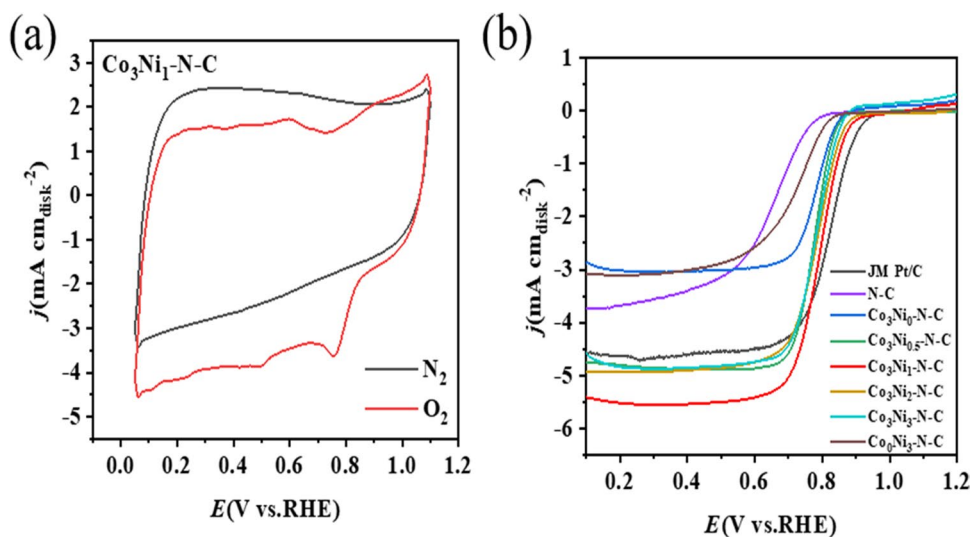
862.6 and 880.2 eV peaks correspond to satellite peaks [40]. The high valence states of Co and Ni indicated the presence of M-Nx bonds, and the presence of metallic Co and Ni peaks confirmed the formation of CoNi alloys in the $\text{Co}_3\text{Ni}_1\text{-N-C}$ sample. The presence of M-Nx and metal Co/Ni was beneficial in the oxygen reaction, and M-Nx is formed due to coordination effects, which optimized the adsorption energy and improved the electrochemical activity. Some other studies have found that for Co-doped samples, moderate amounts of Ni elements could increase the content of Co-Nx species, which also applied to Ni-doped samples. This result suggested that Co/Ni alloys could promote the formation of M-Nx material compared to individual metal-doped samples [41]. In addition, Co and Ni nanoparticles were not isolated from each other but had electronic interactions. In CoNi alloys, Co atoms could obtain d-electrons from nearby Ni atoms, thus increasing the electron-donating properties of the hybrids, which was associated with enhanced electrochemical activity [42]. The above results indicated a modification of the electronic structure between the near-surface Co and Ni atoms [43], suggesting the formation of cobalt–nickel alloys and the presence of bimetallic synergies.

ORR performance testing

First, the ORR performance of the catalysts was characterized using glassy carbon rotating disc electrodes. As shown in Fig. 5a and Fig. S2a–f, the electrocatalysts of catalyst $\text{Co}_x\text{Ni}_y\text{-N-C}$ were tested for CV curves in N_2 and O_2 saturated 0.1 M KOH solutions at 50 mV/s, respectively. Apparently, all the samples did not show oxygen reduction peaks in the N_2 -saturated electrolyte solution, while obvious oxygen reduction peaks appeared in the O_2 -saturated electrolyte solution, which indicated good ORR catalytic activity.

However, it was worth noting that the oxygen reduction peak becomes more positive with the introduction of Co and Ni elements. Among them, the oxygen reduction peak of $\text{Co}_3\text{Ni}_1\text{-N-C}$ appeared around 0.771 V vs. RHE, which was larger than that of the other catalysts of $\text{Co}_x\text{Ni}_y\text{-N-C}$, indicating that the catalytic activity of ORR was improved. To further demonstrate the excellent ORR performance of the catalysts, the LSV curves of the electrocatalysts were recorded by in O_2 -saturated 0.1 M KOH solution at 1600 rpm, as shown in Fig. 5b. It was clearly seen that $\text{Co}_x\text{Ni}_y\text{-N-C}$ catalysts with different Co/Ni molar ratios have different activities, and the electrocatalytic activity of ORR increases with increasing Co and Ni molar ratios. A maximum was reached at a Co/Ni ratio of 3:1, and then the electrocatalytic activity decreased. The results showed that the optimal Co/Ni molar ratio was 3:1, and $\text{Co}_x\text{Ni}_y\text{-N-C}$ had the best ORR catalytic activity, as shown in Fig. 6 where the $\text{Co}_3\text{Ni}_1\text{-N-C}$ electrocatalyst had the largest positive onset potential ($E_0=0.960$ V vs. RHE) and the highest half-wave potential ($E_{1/2}=0.81$ V vs. RHE), which is close to that of commercial Pt/C ($E_0=0.966$ V vs. RHE and $E_{1/2}=0.831$ V vs. RHE). Among the above catalysts, although the ORR performance of the catalysts with only cobalt ($\text{Co}_3\text{Ni}_0\text{-N-C}$) or only nickel ($\text{Co}_0\text{Ni}_3\text{-N-C}$) was improved compared with that of N-C, the enhancement of $\text{Co}_3\text{Ni}_1\text{-N-C}$ activity was more pronounced, suggesting that there was an obvious synergistic catalytic effect of Co/Ni bimetallic in nitrogen-doped carbon matrix. Therefore, it was concluded from the above results that $\text{Co}_3\text{Ni}_1\text{-N-C}$ has excellent ORR electrocatalytic activity. The monometallic cobalt/nickel composites did not show good ORR performance, which could be explained by the strong adhesion of the O^* and OH^* species to the Co/Ni species, which led to a strong activation of the proton transfer step, thus inhibiting the reaction rate [27]. Thus, the presence of CoNi alloy in the graphitic carbon structure

Fig. 5 CV curves of $\text{Co}_3\text{Ni}_1\text{-N-C}$ (a); LSV curves of commercial Pt/C, $\text{Co}_x\text{Ni}_y\text{-N-C}$ and N-C at 1600 rpm (b)



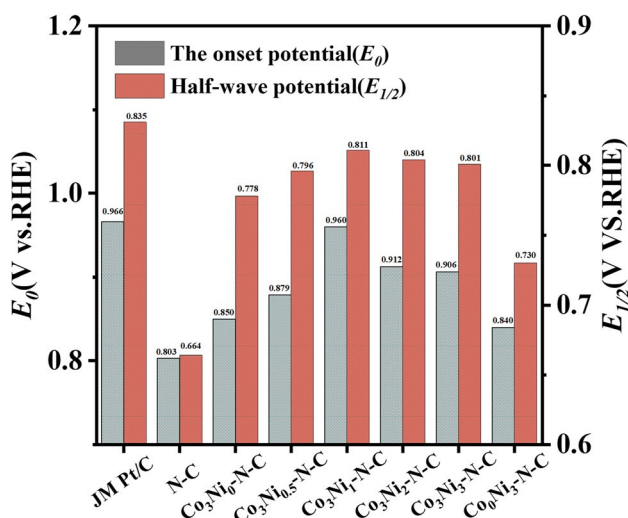


Fig. 6 Histograms of onset and half-wave potentials of commercial Pt/C, $\text{Co}_x\text{Ni}_y\text{-N-C}$ and N-C

helped to promote the electron transfer from the bimetallic alloy to the carbon shell and contributes to the structural modification of the carbon surface, thus improving the catalytic activity of ORR [44].

In order to reveal the ORR kinetics and electron transfer pathways of the catalysts in O_2 -saturated 0.1 M KOH solution, the linear voltammetric scanning curves of $\text{Co}_x\text{Ni}_y\text{-N-C}$ and commercial JM Pt/C measured at different rotational speeds, as shown in Figs. 7 a and c and S3a–l, show that the limiting

diffusion current density keeps increasing with the electrode rotational speed, which indicated that the whole process was controlled by the mass transfer process. In addition, the limiting current density of $\text{Co}_3\text{Ni}_1\text{-N-C}$ ($j_L = 5.5 \text{ mA cm}^{-2}$) at 1600 rpm was superior to that of commercial JM Pt/C ($j_L = 4.6 \text{ mA cm}^{-2}$) and other electrocatalysts of $\text{Co}_x\text{Ni}_y\text{-N-C}$, as shown in Fig. 7a. This suggested that $\text{Co}_3\text{Ni}_1\text{-N-C}$ had excellent ORR kinetics. In order to explore the electron transfer pathway of $\text{Co}_x\text{Ni}_y\text{-N-C}$ in ORR, as Fig. 7 b and d and Fig. S3a–l were the straight lines fitted by K-L equations, the slopes of their K-L straight lines are very close to each other, confirming that this was a first-order oxygen reduction reaction. As shown in Fig. 7 b and d and Fig. S3a–l, the electron transfer number (n) of $\text{Co}_x\text{Ni}_y\text{-N-C}$ at different voltages were also calculated to be about $n = 4.0$ for $\text{Co}_3\text{Ni}_1\text{-N-C}$ and commercial JM Pt/C as shown in Fig. 7b and d, which suggested that $\text{Co}_3\text{Ni}_1\text{-N-C}$ catalysts and commercial JM Pt/C had similar ORR activity and the ORR process is mainly a $4e^-$ pathway. The results showed that most of the oxygen was directly converted to OH^- , including four reaction pathways as follows [45]:

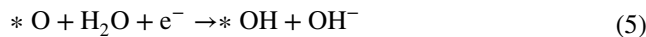
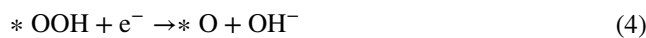
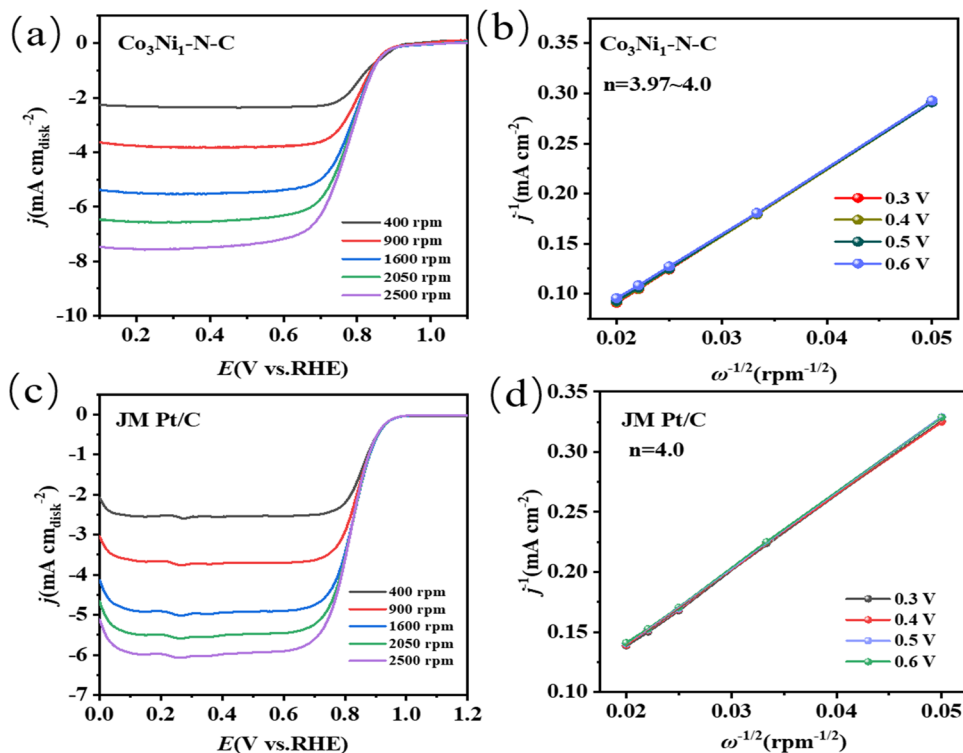


Fig. 7 LSV curves of $\text{Co}_3\text{Ni}_1\text{-N-C}$ and commercial Pt/C at different rotational speeds (a, c); Koutecky-Levich curves and number of transferred electrons for $\text{Co}_3\text{Ni}_1\text{-N-C}$ and commercial Pt/C (b, d)





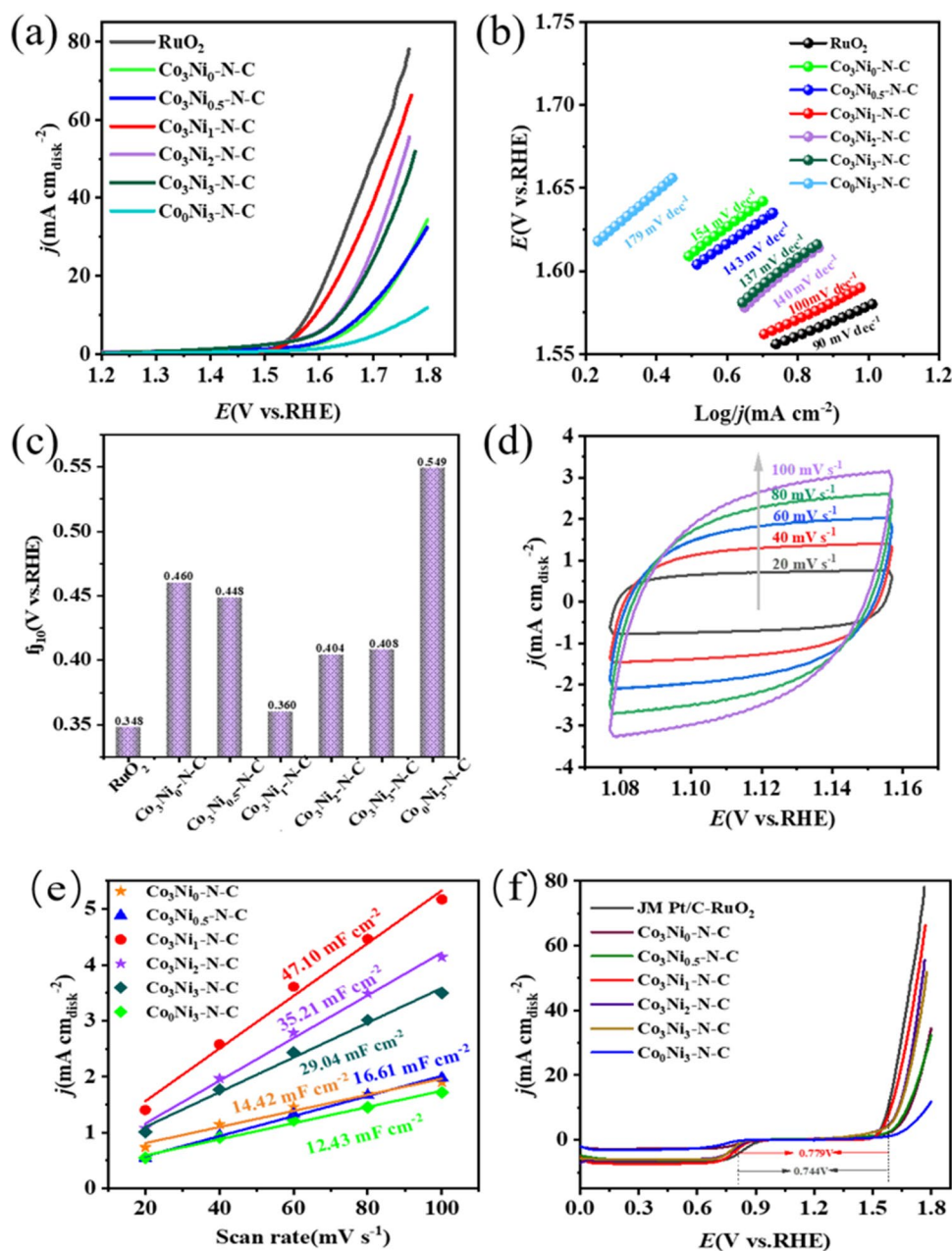
The results showed that the excellent ORR catalytic performance of $\text{Co}_3\text{Ni}_1\text{-N-C}$ electrocatalysts was mainly attributed to the presence of CoNi alloys contributing to the catalytic effect on ORR, the high content of M-N_x and pyridine-N, the unique pleat-rich structure, as well as the large specific surface area and high graphitization.

OER performance testing

The performance of OER was investigated using a glassy carbon rotating disk electrode device. As shown in Fig. 8a,

the LSV curves of the electrocatalysts recorded at 1 M KOH solution, 1600 rpm, it was clear that one of them, $\text{Co}_3\text{Ni}_1\text{-N-C}$, exhibited excellent OER electrocatalytic performance with the smallest overpotential at a current density of 10 mA cm^{-2} ($\eta_{10} = 0.360 \text{ V vs. RHE}$), which was significantly lower than the other $\text{Co}_x\text{Ni}_y\text{-N-C}$ catalysts with overpotentials close to that of commercial RuO_2 ($\eta_{10} = 0.348 \text{ V vs. RHE}$), as shown in Fig. 8c. By determining the Tafel slope, it was evident that the Tafel slope of $\text{Co}_3\text{Ni}_1\text{-N-C}$ (100 mV dec^{-1}) was significantly lower than that of other $\text{Co}_x\text{Ni}_y\text{-N-C}$ catalysts and close to that of commercial RuO_2 (90 mV dec^{-1}), as shown in Fig. 8b, suggesting that $\text{Co}_3\text{Ni}_1\text{-N-C}$ possesses better OER kinetics. To estimate the

Fig. 8 LSV curves of commercial RuO_2 and $\text{Co}_x\text{Ni}_y\text{-N-C}$ at a speed of 1600 rpm (a); Tafel slope curves of commercial RuO_2 and $\text{Co}_x\text{Ni}_y\text{-N-C}$ (b); overpotential η_{10} histograms of commercial RuO_2 and $\text{Co}_x\text{Ni}_y\text{-N-C}$ at 10 mA cm^{-2} (c); CV curves of $\text{Co}_3\text{Ni}_1\text{-N-C}$ at different sweep speeds (d); bilayer capacitance C_{dl} of $\text{Co}_x\text{Ni}_y\text{-N-C}$ (e); LSV curves of commercial Pt/C- RuO_2 and the prepared catalysts at a speed of 1600 rpm (f)



active site of $\text{Co}_x\text{Ni}_y\text{-N-C}$, cyclic voltammetry (CV) curves were recorded at different scan rates ($20\text{--}100\text{ mV s}^{-1}$) as in Fig. 8e and Fig. S4a–f, and the C_{dl} values were measured using CV curves in the non-Faraday region to calculate the electrochemical double-layer capacitance (C_{dl}) as in Fig. 8f. Among them, the C_{dl} value of $\text{Co}_3\text{Ni}_1\text{-N-C}$ was 47.1 mF cm^{-2} , which was significantly higher than that of other $\text{Co}_x\text{Ni}_y\text{-N-C}$ catalysts, such as Co-N-C (14.42 mF cm^{-2}) and Ni-N-C (14.43 mF cm^{-2}), suggesting that $\text{Co}_3\text{Ni}_1\text{-N-C}$ exposed more active sites. The highly coupled N-doped carbon of CoNi alloys provides active sites with high affinity for both reactants and intermediates [46]. Both ORR and OER follow four single electron transfer reactions including a series of intermediates ($^*\text{OH}$, $^*\text{O}$, and $^*\text{OOH}$) [47]. In addition, the electrocatalytic activity of the bifunctional ORR/OER was characterized by calculating the potential difference between the OER and the ORR ($\Delta E = E_{j=10} - E_{1/2}$), which indicates the loss of efficiency. The ΔE value of the apparent $\text{Co}_3\text{Ni}_1\text{-N-C}$ is 0.779 V vs. RHE , as shown in Fig. 8f. Close to the benchmark ΔE value of the combination with commercial noble metal catalysts (Pt/C-RuO₂, 0.744 V vs. RHE) indicates good bifunctional electrocatalytic activity. It was well known that Co and Ni metals themselves were active centers for ORR and OER, respectively; when alloyed with each other, the synergistic effect of Ni and Co makes CoNi nanoparticles better active centers for ORR and OER [48]. These results suggest that this excellent ORR and OER activity is largely due to the unique structure of the folded carbon nanospheres and the synergistic effect between the CoNi nanoparticles and the N carbon-doped carbon layer, which endows $\text{Co}_3\text{Ni}_1\text{-N-C}$ with multiple active sites, accelerates the reaction rate, and reduces the energy of adsorption to the reaction intermediates, which enhanced the ORR/OER electrochemical performance [35].

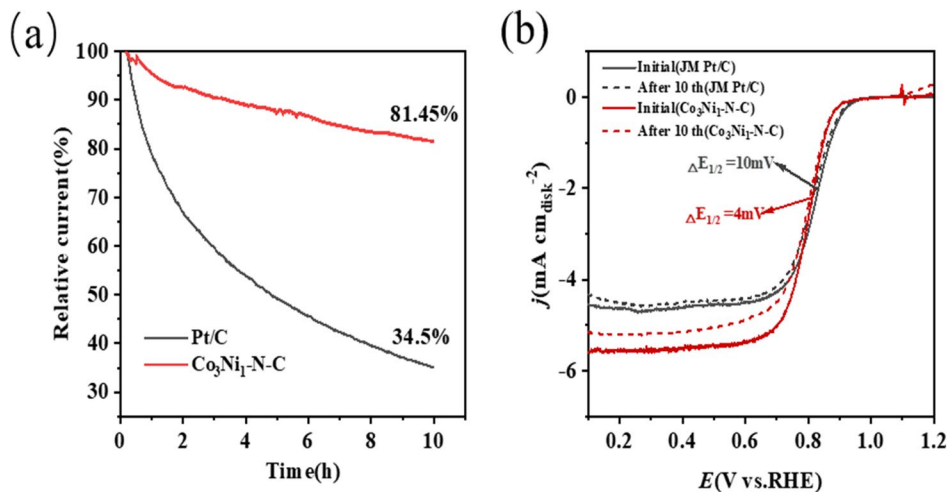
The stability of the electrocatalysts, another key parameter for their potential applications, was tested by

the timed-current method (i-t) for the electrocatalysts $\text{Co}_3\text{Ni}_1\text{-N-C}$, commercial Pt/C and commercial RuO₂. As shown in Figs. 9a and S5a, the relative current of $\text{Co}_3\text{Ni}_1\text{-N-C}$ in 0.1 M KOH solution retained 81.45% of its initial value after 10 h at constant potentials of 0.8 V vs. RHE and 1.6 V vs. RHE , while commercial Pt/C retained only 34.5% under the same conditions, indicating that $\text{Co}_3\text{Ni}_1\text{-N-C}$'s stability was superior to that of commercial Pt/C. As shown in Fig. 9b, the $E_{1/2}$ of $\text{Co}_3\text{Ni}_1\text{-N-C}$ decreased by only 4 mV , whereas that of commercial Pt/C decreased by 10 mV after 10 h . The relative current of commercial RuO₂ in 1 M KOH solution retained 42.10% of its initial value after 8 h , whereas $\text{Co}_3\text{Ni}_1\text{-N-C}$ retained 46.9% under the same conditions, as shown in Fig. S5a. It indicated that $\text{Co}_3\text{Ni}_1\text{-N-C}$ was slightly higher stable than commercial RuO₂ in a solution of 1 M KOH . These results confirmed the excellent durability of CoNi alloy nanoparticles encapsulated by $\text{Co}_3\text{Ni}_1\text{-N-C}$ in N-doped folded carbon nanosphere layers.

In order to elucidate the excellent stability of $\text{Co}_3\text{Ni}_1\text{-N-C}$, the morphology of the electrocatalyst after the stability test was investigated by TEM. As shown in Fig. S6, $\text{Co}_3\text{Ni}_1\text{-N-C}$ retained its initial nanosphere structure after testing in 0.1 M KOH solution, and almost no agglomerations were observed. As shown in Fig. S7, whereas agglomeration of CoNi-based nanoparticles was clearly observed after testing in 1 M KOH solution, which led to a decrease in OER stability due to agglomeration of metal particles as a result of migration at high potentials, overall, the excellent stability of $\text{Co}_3\text{Ni}_1\text{-N-C}$ may be attributed to its unique wrinkled structure.

XPS testing of $\text{Co}_3\text{Ni}_1\text{-N-C}$ after OER stability measurements and the results are shown in Fig. S8. The XPS high-resolution spectra of N1s (Fig. S8a) showed that the peak intensity of pyridine-N was significantly reduced, indicating that pyridine-N, which acted as the active site

Fig. 9 The i-t curves of $\text{Co}_3\text{Ni}_1\text{-N-C}$ and commercial Pt/C in 0.1 M KOH solution at 0.8 V vs. RHE (a); LSV curves of $\text{Co}_3\text{Ni}_1\text{-N-C}$ and commercial JM Pt/C electrocatalysts before and after endurance testing (b)



of the $\text{Co}_3\text{Ni}_1\text{-N-C}$ catalyst during the OER process, partly coordinated with the metal center to form the M-N_x active site, and part of it was oxidized during the reaction process, and a significant enhancement of the M-N_x and oxidized-N peak intensities can also be seen. In addition, the obvious enhancement of the pyrrole-N peak indicates that the metal centers coordinated to the nitrogen atoms in the pyrrole ring are reduced, which decreased the reactivity and selectivity of the catalyst. The XPS spectra of Co 2p (Fig. S8b) showed that there was no obvious change in the position of the peaks of Co, whereas the peak strength of Co^0 of $\text{Co}_2\text{p}_{3/2}$ was reduced. This proved that Co^0 was the active site of $\text{Co}_3\text{Ni}_1\text{-N-C}$ catalyst, which was gradually oxidized during the reaction process, leading to a gradual decrease in catalyst performance. Meanwhile, the XPS spectra of Ni 2p (Fig. S8c) showed that the peak intensity of Ni⁰ decreased and the peak intensity of Ni²⁺ increased for $\text{Ni}2\text{p}_{3/2}$, and basically no Ni⁰ peak was detected in $\text{Ni}2\text{p}_{1/2}$, which indicated that the metallic nickel underwent oxidation or bonding with OH to generate active Ni-OOH intermediate species.

Conclusion

In summary, a carbon nanosphere electrocatalyst, $\text{Co}_x\text{Ni}_y\text{-N-C}$, was successfully synthesized by a soft template method with melamine-assisted pyrolysis. The melamine played a crucial role in the control and distribution of $\text{Co}_x\text{Ni}_y\text{-N-C}$ active sites. The preparation process of $\text{Co}_x\text{Ni}_y\text{-N-C}$ was optimized by adjusting the amount of Co/Ni precursor. The results showed that $\text{Co}_3\text{Ni}_1\text{-N-C}$ exhibit excellent ORR and OER catalytic activities, which should be contributed to the large specific surface area and abundant M-N_x active sites and the synergistic effect of CoNi alloy. In addition, with the addition of Ni, a highly active surface reconstructed Ni-CoOOH layer was formed at a lower potential, which improved the OER catalytic activity. This made it exhibit ORR and OER performance in alkaline electrolytes comparable to that of commercial catalysts. The prepared $\text{Co}_3\text{Ni}_1\text{-N-C}$ catalyst exhibited excellent ORR, OER electrocatalytic performance with a more positive half-wave potential ($E_{1/2} = 0.81$ V vs. RHE), and better long-term stability than that of commercial Pt/C. The catalyst also exhibited a low OER overpotential of 1.60 V. Between ORR and OER, there were advantages for applications in bifunctional electrochemical reactions. Overall, this work showed that the manipulation of catalyst structure and exposed active sites enabled efficient ORR and OER electrocatalysis, which contributed to the design of cost-effective, high-performance bifunctional electrocatalysts.

Supplementary Information The online version contains supplementary material available at <https://doi.org/10.1007/s11581-024-05478-5>.

Author contribution QPZ, LXB, DD, and HBW conceived the central ideas. QPZ and LXB prepared Figs. 1–9. DD and HBW prepared Figures S1–S7. QPZ and LXB wrote the original article. CLL and YYC supervised and revised the paper. All authors reviewed manuscript.

Funding This research was supported by the Gansu Key Research and Development Program (industry field) under Grant No. 23YFGA0056 and Hongliu Outstanding Youth Talents Support Project.

Data availability No datasets were generated or analyzed during the current study.

Declarations

Ethical approval Not applicable.

Competing interests The authors declare no competing interests.

References

- Chen Z, Higgins D, Chen Z (2010) Nitrogen doped carbon nanotubes and their impact on the oxygen reduction reaction in fuel cells. *Carbon* 48(11):3057–3065
- Suntivich J, May KJ, Gasteiger HA, Goodenough JB, Shao Y (2011) A perovskite oxide optimized for oxygen evolution catalysis from molecular orbital principles. *Science* 334(6061):1383–1385
- Deng H, Li Q, Liu JJ, Wang F (2017) Active sites for oxygen reduction reaction on nitrogen-doped carbon nanotubes derived from polyaniline. *Carbon* 112:219–229
- Li Z, Yang H, Cheng W (2023) Recent progress of in situ/operando characterization techniques for electrocatalytic energy conversion reaction. *Chin Chem Lett* 8417(23):109237
- Yu T, Cao X, Song R, Li LZ, Dong X, Li JG, Wang X, Zhou XS, Yuan NY (2023) Ding JN (2023) MOF-derived FeCo-NC@Co₂P-NC as a high-performance bifunctional electrocatalyst for rechargeable Zn-Air batteries. *J Alloys Comp* 939:168679
- Wu X, He DH, Zhang HX, Li H, Li ZJ, Yang B, Lin Z, Lei LC (2016) Zhang X W (2016) Ni_{0.85}Se as an efficient non-noble bifunctional electrocatalyst for full water splitting. *Int J Hydrogen Energy* 41(25):10688–94
- Alonso VN, Feng Y (2019) Yang H (2019) Novel non-precious metal electrocatalysts for oxygen electrode reactions. *Catalysts* 9(9):731
- Chen L, Xu ZX, Han WJ, Zhang Q, Bai ZY, Chen Z, Li G, Wang XL (2020) Bimetallic CoNi alloy nanoparticles embedded in pomegranate-like nitrogen-doped carbon spheres for electrocatalytic oxygen reduction and evolution. *ACS Appl Nano Mater* 3(2):1354–1362
- Chen X, Li YH, Zhao XY (2023) Screening of transition metal-based MOF as highly efficient bifunctional electrocatalysts for oxygen reduction and oxygen evolution. *Surf Interf* 38:102821
- Lu X, Wang T, Cao M, Cheng W (2023) Homogeneous NiMoO₄-Co(OH)₂ bifunctional heterostructures for electrocatalytic oxygen evolution and urea oxidation reaction. *Int J Hydrogen Energy* 48(89):34740–34749
- Das SK, Kesh A, Akula S, Akula S, Panda SK, Kiruthika GVM, Sahu AK (2022) Co-, Ni-catalyzed borylation of carbon nanofibers for oxygen reduction reaction in an anion exchange membrane fuel cell. *ACS Appl Energy Mater* 5(8):10240–10253

12. Liu MY, Xiao XD, Li Q, Luo LY, Ding MH, Zhang B, Li YX, Zou JL, Jiang BJ (2022) Recent progress of electrocatalysts for oxygen reduction in fuel cells. *J Colloid Interface Sci* 607(1):791–815
13. He CS, Zhang TT, Sun FZ, Li CQ (2017) Lin Y Q (2017) Fe/N co-doped mesoporous carbon nanomaterial as an efficient electrocatalyst for oxygen reduction reaction. *Electrochim Acta* 231:549–556
14. Liu S, Xiao L, Wang G, Liu Y, Mo Y, Lu W (2023) Heteroatom-doped carbon materials from bimetal covalent organic polymers as efficient bifunctional electrocatalysts in oxygen reduction and oxygen evolution reactions. *Mater Today Sustain* 22:100389
15. Wu T, Sun M-Z, Huang B-L (2022) Non-noble metal-based bifunctional electrocatalysts for hydrogen production. *Rare Met* 41(7):2169–2183
16. Cheng W, Wang H, Gu Z (2024) Modulation of the electronic structure of CoP by surface and interface codoping boosts electrocatalytic oxygen evolution reaction [J]. *Int J Hydrogen Energy* 51:914–921
17. Zhang XJ, Chen YF, Wang B, Chen ML, Yu B, Wang XQ, Zhang WL, Yang DX (2019) FeNi nanoparticles embedded porous nitrogen-doped nanocarbon as efficient electrocatalyst for oxygen evolution reaction. *Electrochim Acta* 321:134720
18. Liu ZZ, He TZ, Jiang QQ, Wang W, Tang JG (2022) A review of heteroatomic doped two-dimensional materials as electrocatalysts for hydrogen evolution reaction. *Int J Hydrogen Energy* 47(69):29698–29729
19. Kundu A, Bolar S, Das S, Kolya H, Kang C-W, Kuila T, Murmu NC (2022) General approach to synthesize multilayer graphitic carbon-nanotube-encapsulated NiCo alloys as trifunctional electrocatalysts: deciphering the role of N-dopants. *ACS Appl Energy Mater* 5(11):14445–14454
20. Li H, Du ZY, He F, Chen SQ, Yang HH, Tang KW (2023) Cobalt carbonate hydroxide assisted formation of self-supported CoNi-based metal–organic framework nanostrips as efficient electrocatalysts for oxygen evolution reaction. *Int J Hydrogen Energy* 48(41):15566–15573
21. Yang C, Wang H-B, Liang P, Wu B-F, Zhao L, Leng P-S, Lv L, Wan H-Z, Wang H (2023) Size and structure tuning of FePt nanoparticles on hollow mesoporous carbon spheres as efficient catalysts for oxygen reduction reaction. *Rare Met* 42(6):1865–1876
22. Qu HQ, Ma YR, Li XL, Duan YH, Li Y, Liu F, Yu B, Tian MG, Li ZJ, Yu YQ, Lv ZG, Wang L (2023) Ternary alloy (FeCoNi) nanoparticles supported on hollow porous carbon with defects for enhanced oxygen evolution reaction. *J Colloid Interface Sci* 645:107–14
23. Lee J, Kim JG, Pak C (2021) Electrolyte accessibility of non-precious-metal catalysts with different spherical particle sizes under alkaline conditions for oxygen reduction reaction. *J Energy Chem* 52:326–331
24. Cong YY, Xie GH, Meng XZ, Wang HB, Meng FC, Li CL (2021) Zhao Q P (2021) Melamine-assisted synthesis of atomically dispersed Fe sites anchored on crumple-rich carbon nanospheres as highly efficient electrocatalysts for oxygen reduction reaction. *Ionics* 27(12):5287–5295
25. Huang SJ, Zhang W, Chen Q, Zhou S, Sun L, Sha LN, Zhang GL, Wang P, Han XG (2023) N-doped carbon confined NiCo alloy hollow spheres as an efficient and durable oxygen electrocatalyst for zinc-air batteries. *Chem-A Eur J* 29(30):e202300321
26. Mahmood A, Xie NH, Zhao BL, Zhao BL, Zhong LJ, Zhang YW, Niu L (2023) Optimizing surface N-doping of Fe-N-C catalysts derived from Fe/melamine-decorated polyaniline for oxygen reduction electrocatalysis. *Adv Mater Interfaces* 8(13):2100197
27. Fan FF, Huang QL, Rani KK, Peng XL, Liu XT, Wang LM, Yang ZY, Huang DJ, Devasenathipathy R, Chen D-H, Fan YJ, Chen W (2023) Interface and doping engineering of Co-based electrocatalysts for enhanced oxygen reduction and evolution reactions. *Chem Eng J* 470:144380
28. Zhu H, Dai YJ, Di SX, Tian L, Wang FH, Wang ZQ, Lu YH (2023) Bimetallic ZIF-based PtCuCo/NC electrocatalyst Pt Supported with an N-doped porous carbon for oxygen reduction reaction in PEM fuel cells. *ACS Appl Energy Mater* 6(3):1575–84
29. Kundu A, Samanta A, Raj CR (2021) Hierarchical hollow MOF-derived bamboo-like N-doped carbon nanotube-encapsulated Co_{0.25}Ni_{0.75} alloy: an efficient bifunctional oxygen electrocatalyst for zinc–air battery. *ACS Appl Mater Interfaces* 13(26):30486–96
30. Zhang HB, Zhou W, Lu XF, Chen T, Lou XW (2020) Implanting isolated Ru atoms into edge-rich carbon matrix for efficient electrocatalytic hydrogen evolution. *Adv Energy Mater* 10(23):2000882
31. Lee G, Kim J (2023) Oxygen evolution catalyst containing CoNi nanoalloy and carbon nanotube maximized the electrochemical surface area and intrinsic activity. *Solid State Sci* 135:107063
32. Liu H, Hua D, Wang R, Liu ZG, Li JJ, Wang XJ, Song B (2022) High-performance bifunctional oxygen electrocatalysts for zinc-air batteries over nitrogen-doped carbon encapsulating CoNi nanoparticles. *J Phys D Appl Phys* 55(48):484005
33. Fan HF, Wang T, Gong H, Jiang C, Sun ZP, Zhao MM, Song L, He JP (2021) Heteroatom sulfur-induced defect engineering in carbon nanotubes: enhanced electrocatalytic activity of oxygen reduction reaction. *Carbon* 180:31–40
34. Shao CK, Luo MS, Song HQ, Zhang SX, Wang FL, Liu XY, Huang ZT (2023) Highly active porous carbon-supported CoNi bimetallic catalysts for four-electron reduction of oxygen. *Energy Fuels* 37(5):4026–4037
35. Yang L, Wang D, Lv YL, Cao DP (2019) Nitrogen-doped graphitic carbons with encapsulated CoNi bimetallic nanoparticles as bifunctional electrocatalysts for rechargeable Zn–Air batteries. *Carbon* 144:8–14
36. Bhardwaj SS, Kapse S, Dan S, Thapa R, Dey RS (2023) Elucidating the oxygen reduction reaction kinetics on defect engineered nanocarbon electrocatalyst: interplay between the N-dopant and defect sites. *J Mater Chem A* 32:17045–17055
37. Guo SJ, Yang YM, Liu NY, Qiao S, Huang H, Liu HH, Liu Y, Kang ZH (2016) One-step synthesis of cobalt, nitrogen-codoped carbon as nonprecious bifunctional electrocatalyst for oxygen reduction and evolution reactions. *Sci Bull* 61(1):68–77
38. Kumar G, Dey RS (2023) Coordination engineering of dual Co, Ni active sites in N-doped carbon fostering reversible oxygen electrocatalysis. *Inorganic Chem* 62(33):13519–29
39. Liu Y, Chen ZC, Li ZX, Zhao N, Xie YL, Du Y, Xuan JN, Xiong DB, Zhou JQ, Cai L, Yang YH (2022) CoNi nanoalloy-Co-N₄ composite active sites embedded in hierarchical porous carbon as bi-functional catalysts for flexible Zn-air battery. *Nano Energy* 99:107325
40. Jiang M, Yang J, Ju J, Zhang W, Lin He, Zhang J, Fu CP, Sun B (2020) Space-confined synthesis of CoNi nanoalloy in N-doped porous carbon frameworks as efficient oxygen reduction catalyst for neutral and alkaline aluminum-air batteries. *Energy Storage Mater* 27:96–108
41. Kim K, Min K, Go YH, Lee Y, Shim SE, Lim DW, Baek S-H (2022) FeCo alloy nanoparticles embedded in N-doped carbon supported on highly defective ketjenblack as effective bifunctional electrocatalysts for rechargeable Zn–air batteries. *Appl Catal B* 315:121501
42. Ning HH, Li GQ, Chen Y, Zhang KK, Gong Z, Nie RF, Hu W, Xia QH (2019) Porous N-doped carbon-encapsulated CoNi alloy nanoparticles derived from MOFs as efficient bifunctional oxygen electrocatalysts [J]. *ACS Appl Mater Interfaces* 11(2):1957–1968
43. Li JJ, Qian JQ, Chen XY, Zeng XX, Li L, Ouyang B, Kan E, Zhang WM (2022) Three-dimensional hierarchical graphitic carbon encapsulated CoNi alloy/N-doped CNTs/carbon nanofibers as

- an efficient multifunctional electrocatalyst for high-performance microbial fuel cells. *Compos B Eng* 231:109573
44. Wei D, Chen LX, Tian LD, Ramakrishna S, Ji DX (2023) Melamine-derived carbon foam-supported graphene-CoNi nanocomposites as high-performance OER/HER bifunctional electrocatalysts [J]. *J Chem Technol Biotechnol* 98(4):910–918
 45. Zhang CL, Wang BW, Shen XC, Liu JW, Kong XK, Chuang SSC, Yang D, Dong A, Peng ZM (2016) A nitrogen-doped ordered mesoporous carbon/graphene framework as bifunctional electrocatalyst for oxygen reduction and evolution reactions. *Nano Energy* 30:503–510
 46. Mehek R, Iqbal N, Noor T, Ghazi ZA, Umair M (2022) Metal-organic framework derived vanadium oxide supported nanoporous carbon structure as a bifunctional electrocatalyst for potential application in metal air batteries. *RSC Adv* 13(1):652–664
 47. Wang HF, Tang C, Zhang Q (2018) A review of precious-metal-free bifunctional oxygen electrocatalysts: rational design and applications in Zn-Air batteries. *Adv Func Mater* 28(46):1803329
 48. Chen D, Zhu JW, Mu XQ, Cheng RL, Li WQ, Liu SL, Pu ZH, Lin C, Mu SC (2022) Nitrogen-Doped carbon coupled FeNi₃ intermetallic compound as advanced bifunctional electrocatalyst for OER, ORR and zn-air batteries. *Appl Catal B* 268:118729

Publisher's Note Springer Nature remains neutral with regard to jurisdictional claims in published maps and institutional affiliations.

Springer Nature or its licensor (e.g. a society or other partner) holds exclusive rights to this article under a publishing agreement with the author(s) or other rightsholder(s); author self-archiving of the accepted manuscript version of this article is solely governed by the terms of such publishing agreement and applicable law.